

3D Convolutional Autoencoder (3D-CAE) Feature Engineering for Sea Ice Surface Roughness,  
Thickness and Type Extractions from RADARSAT-2 Synthetic Aperture Radar (SAR)

by

Sangwon Lim (V00923765)

sangwonl@uvic.ca

CSC497: Interdisciplinary Project

Geomatics (Geography & Computer Science)

University of Victoria

Victoria, BC, Canada

Dec / 19 / 2021

3D Convolutional Autoencoder (3D-CAE) Feature Engineering for Sea Ice Surface Roughness, Thickness and Type Extractions from RADARSAT-2 Synthetic Aperture Radar (SAR) Data

**Table of Contents**

Abstract .....	01
Introduction .....	01
Methods .....	02
Study Area and Data Preprocessing .....	02
Kernel-based Feature Engineering .....	04
3D-CAE Feature Engineering .....	05
Training Models .....	07
Model Evaluation .....	07
Results .....	08
3D-CAE Feature Engineering .....	08
MYI-FYI Classification .....	08
Surface Roughness Regression .....	09
Thickness Regression .....	10
Discussion .....	12
Conclusion .....	13
Acknowledgement .....	13
References .....	14

### **Abstract**

While precise sea ice feature extractions of surface roughness and thickness have been accomplished using Radar/laser altimetry data with a meagre temporal resolution, the performances obtained using SAR data were not satisfactory. This study aims to close the gap by applying state-of-the-art 3D Convolutional Autoencoder (3D-CAE) feature engineering on RADARSAT-2 data. It is an initiative work that can provide insights into the potential applicability of RADARSAT Constellation Mission (RCM) data in sea ice research. The autoencoding is processed on multiple  $7 \times 7$  window stacks, and a feature reduction of 93.75% with ~90% information preservation is achieved using the developed architecture. Sobel and Canny edge detection layers are calculated and added to the window stacks. The encoded features are concatenated with other processed features to be fed into a Deep Neural Network. The results are compared with several kernel-based feature engineering methods, such as the standard deviation of backscatter values, coefficient correlation between HH and HV, and Grey-level Co-occurrence Matrix products in a sliding window. Observations suggest that 3D-CAE features outperform other methods in First-Year Ice (FYI) surface roughness estimation and classification between FYI and Multi-Year Ice (MYI). The applicability of 3D-CAE feature engineering in thickness extraction should be further investigated for enhancement.

### **Introduction**

Sea ice surface roughness, thickness and type feature extractions have been researched in many studies due to their growing importance in polar navigation/exploration, earth science research and recent decades' climate changes (Cafarella et al., 2019; Karvonen, 2012b; Kim et al., 2011; Kwok et al., 2009; Lee et al., 2016; Liu et al., 2015; Petty et al., 2020; Ressel et al., 2015; Su et al., 2018). However, most sea ice is in the polar regions where human accessibility is significantly low. To overcome the obstacle, space-borne remote sensing technology has been tested for its applicability in the field. For example, multiple studies have achieved successful sea ice thickness extractions using altimetry data from ICESat and CryoSat missions (Kwok et al., 2009; Lee et al., 2016; Landy et al., 2020; Petty et al., 2020). The high accuracy results from detecting the sea ice freeboard from the data. Nevertheless, such methods cannot maximize the utility with poor data continuity: the revisit cycles are 91 days and 369 days for ICESat-2 and CryoSat, respectively. On the contrary, Synthetic Aperture Radar (SAR) data are far more abundant, making it an alternative for sea ice feature extractions. This study's primary objective is to optimize sea ice feature extractions taking advantage of RADARSAT-2 data. Assessments on the methods may propose their potential applicability on the RADARSAT Constellation Mission (RCM) data. The temporal resolution of the RCM data is only four days revisited by three satellites launched in 2019.

Extractions of three sea ice features, surface roughness and thickness, using deep learning methods are the main focus of this study, with a peripheral goal on First-Year Ice (FYI) and Multi-Year Ice (MYI) classification. Developed methods aim at enhancing the foundation knowledge

from previous studies about feature extractions from SAR data. Cafarella et al. (2019) discovered a strong positive correlation of ( $r=0.86$ ) between RADARSAT-2 C-band HH-polarization backscatter (HH) and FYI roughness in winter and a strong negative correlation ( $r=-0.83$ ) HV/HH ratio and FYI roughness in the advanced melt season. Observations by Kim et al. (2012) suggest a potential one-to-one relationship between the fast sea ice thickness and depolarization factors from C and X bands from TerraSAR-X and RADARSAT-2. Co-polarized correlation and cross-polarization ratio features recorded a strong correlation,  $0.76 < r < 0.88$ , with sea ice thickness data. Karvonen et al. (2012) developed a sea ice thickness estimation model using data from RADARSAT missions, which is assisted by a sea ice thermodynamic model, HIGHTSI. The method requires high-resolution atmospheric forcing and inputs from processed SAR features. One input is sea ice concentration estimation derived from absolute gradient calculation. While its application in remote sensing is yet to be explored, Canny edge detection is better at absolute gradient approximation for image mining than Sobel detection, according to Ahmed (2018), Vijayarani and Vinupriya (2013). Gray-Level Co-occurrence Matrix (GLCM) texture features on X-band SAR images for sea ice type classification have been experimented with and showed promising results by Ressel et al. (2015).

Many of the methods mentioned above are kernel-based feature extractions involving sliding window operations, which showed satisfactory performance. However, the operations are performed on a single window, which cannot account for distinctive inter-window convolutional relationships. This study proposes an unsupervised deep 3-dimensional Convolutional Autoencoder (3D-CAE) feature engineering technique to extract an inter-window convolutional representation of a multi-window stack. The method's applicability in polarimetric SAR Remote Sensing has been discovered by Shang et al. (2019) for crop type classification with 3D-CAE using  $12 \times 12$  L-band kernel inputs, which showed better results than other available methods.

Different sea ice surface roughness and thickness estimation performance results are compared using basic backscatter features with other kernel-based features, such as the co-polarized correlation between HH and HV, the standard deviation of backscatter values, GLCM products and 3D-CAE features from a sliding window. Different data window combinations are stacked to train 3D-CAEs. Experiments are performed separately on FYI, MYI and combined datasets. Optimal methods are identified using multiple regression model evaluation metrics.

## Methods

### Study Area and Data Preprocessing

Data are collected in the Canadian Arctic Archipelago (CAA), focusing on the McClintock channel. Airborne Electromagnetic (AEM) surveys took place in late April or early May in 2015, 2016 and 2018 (Figure 1). Roughness and thickness expert data are collected from the surveys.

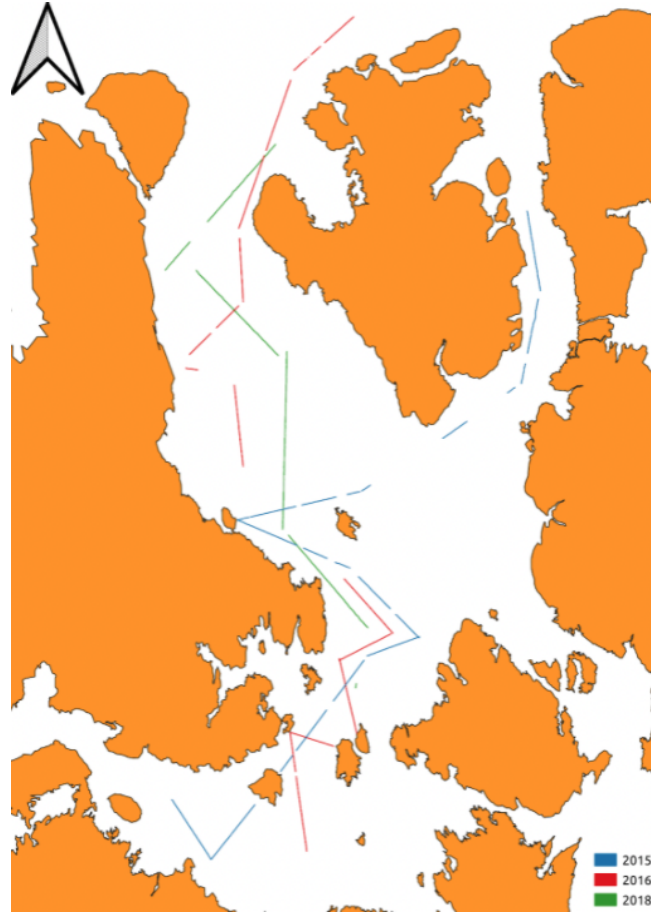


Figure 1. Flight lines of AEM data collections in 2015, 2016 and 2018.

Surface roughness data are collected using Riegl LMS Q120 NIR laser scanner with approximately 1m interval between data points. The sensor detects vertical surface heights relative to a fitted flat surface, which is the standard deviation in millimetres. An EM-Bird laser altimeter instrument collected thickness data in meters at every ~6m point interval along the flight lines.

Multiple RADARSAT-2 C-band data collected with ScanSAR mode from March to April are aggregated into 2015, 2016 and 2018 images with 100m $\times$ 100m spatial resolution. The numbers of SAR images aggregated for the composite images are 76, 81 and 74, respectively. Pixel values represent the averages of overlapping HH, HV and incidence angle values at the location. Training data are extracted from 2015 and 2016 images, and test data are strictly sourced from 2018 images. Having different sources for training-test dataset split is to mitigate the effect of spatial and temporal autocorrelation when testing the model. Surface roughness and thickness data points within a pixel are averaged for the generalized representation of expert data. One problem with this generalization is its inability in representing the actual expert data since data points are not randomly distributed spatially in a pixel. The linearly gathered points may result in a bias towards spatial autocorrelation. Therefore, limiting the minimum number of data points for aggregation is essential to reduce the confidence interval while preserving a sufficient amount of training samples.

The number of surface roughness data points within a pixel is limited to 50, resulting in 8719 training samples and 1012 test samples. Setting the thickness data threshold to 10 points per pixel creates training and test dataset sizes of 9969 and 3422, respectively. Datasets are split further into FYI and MYI datasets with an experienced sea ice expert's assistance (Figure 2; Table 1).

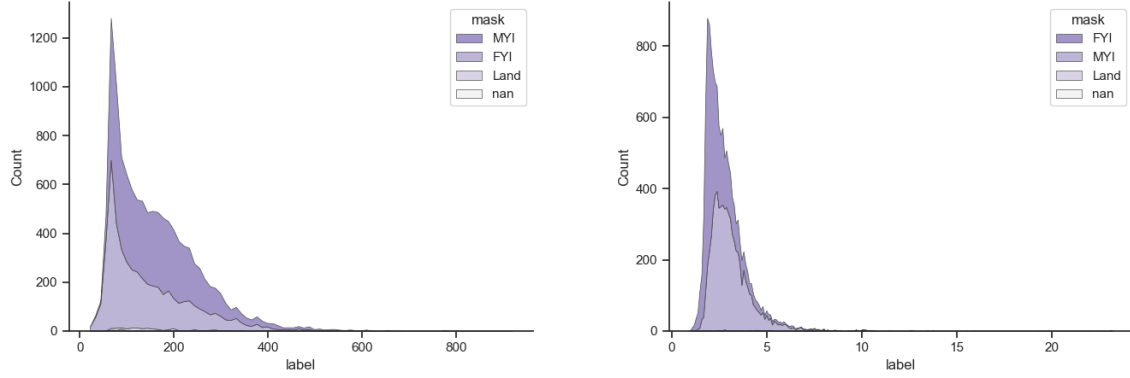


Figure 2. Histograms of surface roughness and thickness datasets.

Table 1. Surface roughness and thickness dataset sizes

		Combined	FYI	MYI
Surface Roughness	Training	8,719	4,049	4,531
	Test	3,235	1,012	2,161
Thickness	Training	9,969	5,123	4,766
	Test	3,422	1,106	2,316

### Kernel-based Feature Engineering

A kernel is a square-shaped sliding window with a pixel of interest at the center. The most straightforward kernel-based feature extraction is the standard deviations of HH and HV backscatter values in sliding windows (Equation 1). Window sizes of  $5 \times 5$ ,  $7 \times 7$  and  $9 \times 9$  are used; thus, six features are created.

$$\sigma = \sqrt{\frac{\sum_{i,j=1}^n (x_{i,j} - \mu)^2}{n^2}} \quad (\text{Equation 1})$$

Where,

$\sigma$  = standard deviation of HH or HV values in a sliding window

$n$  = height or width of a sliding window

$x_{i,j}$  = HH or HV value at  $(i, j)$  in a sliding window

$\mu$  = Mean of HH or HV values in a sliding window

The correlation coefficients (Pearson's  $r$ ) between HH and HV values are also calculated in the same windows, appending three additional features (Equation 2).

$$r = \frac{\sum_{i,j=1}^n (HH_{i,j} - \overline{HH})(HV_{i,j} - \overline{HV})}{\sqrt{\sum_{i,j=1}^n (HH_{i,j} - \overline{HH})^2 \cdot \sum_{i,j=1}^n (HV_{i,j} - \overline{HV})^2}} \quad (\text{Equation 2})$$

Where,

r = Pearson's r between HH and HV

n = height or width of a sliding window

HH<sub>i,j</sub> = HH value at (i, j) in a sliding window

HV<sub>i,j</sub> = HV value at (i, j) in a sliding window

A Gray-Level Co-occurrence Matrices (GLCM) are 2-dimensional histograms that hold the counts of all possible neighbouring pixel value pairs in a sliding window in eight directions: North, Northeast, East, Southeast, South, Southwest, West and Northwest. The histogram size is 256×256, where columns and rows represent the origin and target pixels values. Therefore, the HH and HV images should be rescaled to the integer range of 0 to 256. GLCMs generated for all eight directions are then summed element-wise. Six texture features are generated using the resulting matrix (Equations 3, 4, 5, 6, 7 and 8) (Haralick et al., 1973).

$$Contrast = \sum_{i,j=1}^{256} P_{i,j} (i - j)^2 \quad (\text{Equation 3})$$

$$Dissimilarity = \sum_{i,j=1}^{256} P_{i,j} |i - j| \quad (\text{Equation 4})$$

$$Homogeneity = \sum_{i,j=1}^{256} \frac{P_{i,j}}{1 + (i-j)^2} \quad (\text{Equation 5})$$

$$ASM = \sum_{i,j=1}^{256} P_{i,j} \quad (\text{Equation 6})$$

$$energy = \sqrt{ASM} \quad (\text{Equation 7})$$

$$correlation = \sum_{i,j=1}^{256} \left[ \frac{(i-\mu_i)(j-\mu_j)}{\sqrt{\sigma_i^2 \cdot \sigma_j^2}} \right] \quad (\text{Equation 8})$$

Where,

P<sub>i,j</sub> = GLCM histogram count at (i, j)

μ<sub>i</sub> and μ<sub>j</sub> = means of P<sub>i</sub> column and P<sub>j</sub> row

σ<sub>i</sub> and σ<sub>j</sub> = standard deviations of P<sub>i</sub> column and P<sub>j</sub> row

### 3D-CAE Feature Engineering

The proposed 3D-CAE architecture takes a 8×8×n input and outputs a window stack with the same dimension sizes, where n is the number of windows. A zero padding is appended to the first two dimensions, x- and y-axes, as the window size of 7×7 is used to have the pixel of interest in the

center. Three autoencoders are trained using different window stacks: Stack 1) stacking HH and HV windows wrapped with the same incidence angle windows at the bottom and top, Stack 2) adding HH and HV Sobel edge detected windows above and below the first window stack, and Stack 3) adding HH and HV Canny edge detected windows the first window stack (Figure 3).

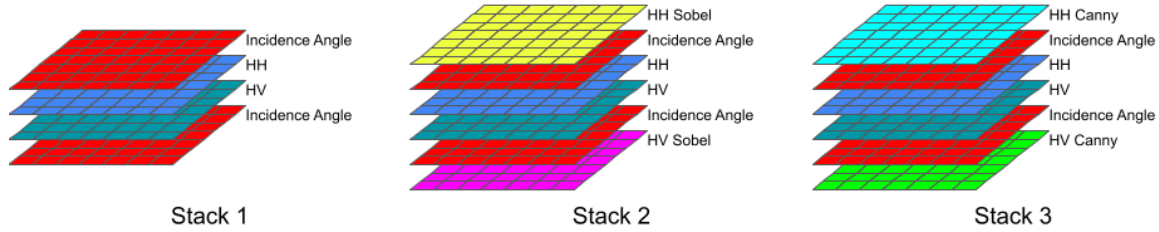


Figure 3. Three window stacks for training 3D-CAEs.

The second and third stacks require zero paddings added at the third dimension, z-axis, to complete the window stack height of power of two (i.e.  $2^3=8$ ). The zero-padding processes allow the 3D-CAE's ability for original dimension reconstruction using  $2 \times 2 \times 2$  Max-pooling and Up-sampling (Figure 4). The rectified linear activation unit (ReLU) was used for all 3D convolution layers except for the very last layer, which uses the sigmoid activation. Extra zero paddings are applied before each convolution layer to maintain the same x and y dimensions before and after. Adam optimization is applied for training the 3D-CAE. The output window stack gets similar to the input throughout the training iterations. Only the encoding process is detached from the autoencoder once training is finished. The dimension reduction using the autoencoder is 93.75% using the developed architecture. The encoded features are then flattened into a vector and concatenated with other features to be fed into a Deep Neural Network.

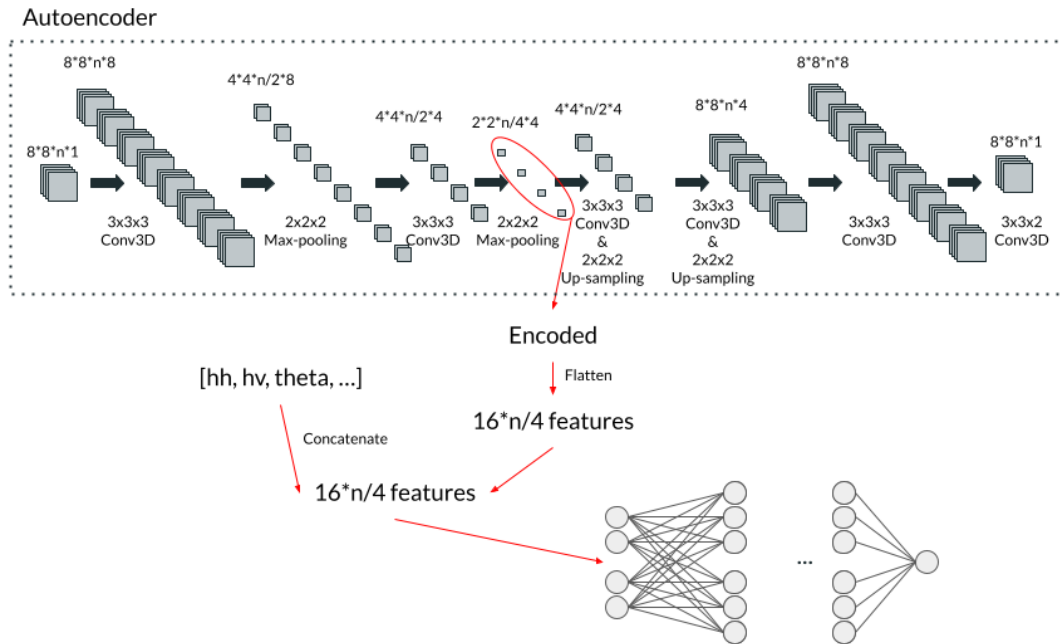


Figure 4. Illustration of 3D-CAE feature engineering combined with Neural Network training process.

The autoencoder consists of encoding (left half) and decoding (right half) processes.



## Training Models

Deep Neural Network with five hidden layers is developed to perform surface roughness and thickness regressions on FYI, MYI and the combined datasets. The hidden dense layer size was determined using Heaton's rules of thumb (Heaton, 2017). The regression architecture has only one neuron for its output layer. On the other hand, the FYI-MYI classification requires two perceptrons with Softmax activation in the output layer.

All features except for the expert data are min-max normalized so that all values fall in the range between 0 and 1 (Equation 9). The standard maximum and minimum values are from the training dataset extracted from 2015 and 2016 images. The test dataset from the 2018 image is normalized using the same minimum and maximum values. Therefore, there may be some values out of the range.

$$normalized = \frac{original - min_{tr}}{max_{tr} - min_{tr}} \quad (\text{Equation 9})$$

Sea ice surface roughness and thickness regressions are trained separately on FYI, MYI and combined training datasets with K-fold validation where K=10. There are six different feature sets experimented on for each regression and FYI-MYI classification problem.

*F1 (backscatter)*: HH, HV, HH/HV ratio and incidence angle

*F2 (corr\_std)*: Kernel-based correlation coefficients and standard deviations added to F1)

*F3 (GLCM)*: GLCM features added to F2)

*F4 (CAE)*: 3D-CAE features trained Stack 1 added to F2)

*F5 (SOBEL\_CAE)*: 3D-CAE features trained with Stack 2 added to F2)

*F6 (canny\_CAE)*: 3D-CAE features trained with Stack 3 added to F2)

## Model Evaluation

Models trained using different feature sets are compared for each regression and classification problems. Root Means Squared Error (RMSE) and  $R^2$  score are the evaluation metrics of regression models (Equations 10 and 11). By having the variance of predicted values as a denominator, a higher  $R^2$  score indicates that a model's performance did not result from simply fitting to a small range of prediction values. The accuracies of classification models help identify ones with better performances (Equation 12).

$$RMSE = \sqrt{\frac{\sum(predicted - expert)^2}{N}} \quad (\text{Equation 10})$$

$$R^2 = 1 - \frac{\sum(predicted - expert)^2}{variance(prediction)} \quad (\text{Equation 11})$$

$$Accuracy = \frac{MYI_{accurate} + FYI_{accurate}}{N} \quad (\text{Equation 12})$$

Where N = number of test samples

## Results

### 3D-CAE Feature Engineering

All six 3D-CAEs trained using surface roughness and thickness training datasets with three kernel-stacks were successful in preserving the original data with Mean Absolute Errors (MAEs) lower than 0.12 (Table 1). Since the original data are Min-Max normalized (range: 0~1), the MAEs could be interpreted as the information loss in percentage. The results show that encoding a  $7 \times 7 \times 4$  window stack, Stack 1, loses more information than Stacks 2 and 3 with the third dimension size of 6.

Table 2. MAEs between data using 3D-CAEs and Min-Max normalized data.

Dataset	Stack 1	Stack 2	Stack 3
Surface Roughness	0.108	0.068	0.046
Thickness	0.118	0.024	0.048

### FYI-MYI Classification

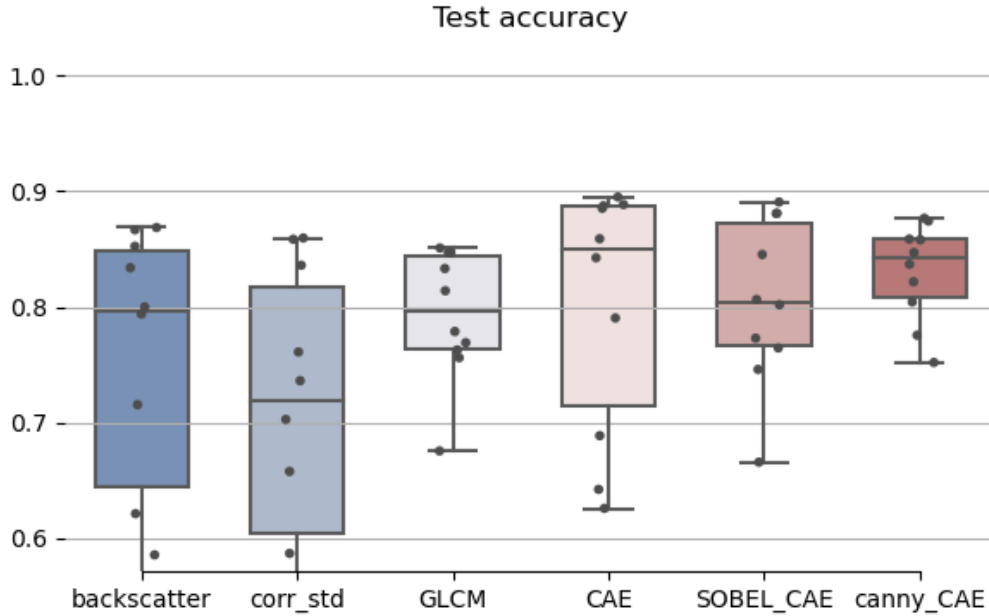


Figure 5. FYI-MYI classification accuracies of different models

While the *GLCM* method suggested by Ressel et al. (2015) shows a better performance than *backscatter* and *corr\_std* methods with an average accuracy of 79.34%, the highest maximum and average accuracies are resulted from using 3D-CAE features (Figure 5). Overall, the highest accuracy of 89.48% is from the model using 3D-CAE features trained without absolute gradient approximation (*F4*), while the highest average of 83.04% is obtained using 3D-CAE features trained with Canny edge detection (*F6*) (Table 3). Lower variances in results occur when 3D-CAEs are trained with absolute gradient approximations (*F4* and *F5*), where the *canny\_CAE* recorded the lowest standard deviation of 4.2%.

Table 3. Maximum, Average and Standard Deviation (SD) of resulting classification accuracies.

	F1	F2	F3	F4	F5	F6
Maximum	86.85%	85.95%	85.08%	89.49%	89.05%	87.65%
Average	74.72%	71.30%	79.34%	80.04%	80.54%	83.04%
SD	12.50%	11.58%	5.58%	10.78%	7.15%	4.20%

### Surface Roughness Regression

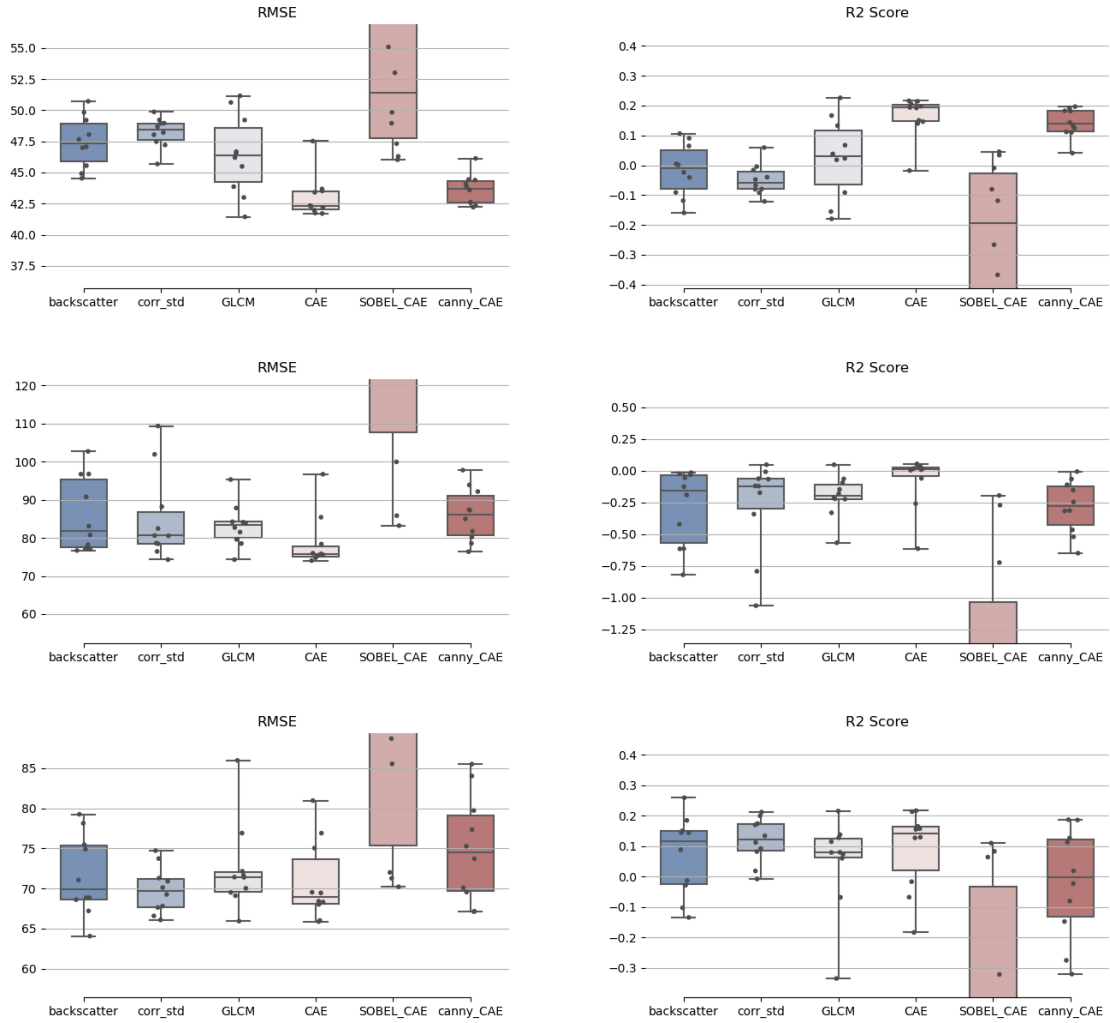


Figure 6. RMSEs (left) and R<sup>2</sup> scores (right) of sea ice surface roughness regression models trained with FYI (top), MYI (middle) and combined (bottom) datasets.

Sea ice surface roughness regression models trained using FYI, MYI and combined datasets are tested (Figure 6). *CAE* and *canny\_CAE* models trained with Stack 1 and Stack 3 outperform other models with average RMSEs of 43.03mm and 43.62mm, respectively. Their average R<sup>2</sup> scores are 0.1640 and 0.1417, the two highest of all results. For the MYI results, the lowest average and minimum RSMEs are 78.72mm and 74.05mm, both obtained from the *CAE* models. The highest

average and maximum  $R^2$  scores of -0.0776 and 0.0535 are also from the same models. In contrast, the trend of *CAE* models showing better performances is not prominent in predicting sea ice surface roughness in the combined dataset. The *corr\_std* model recorded the best average RMSE and  $R^2$  score of 69.81mm and 0.1182, with the lowest standard deviations of 2.91mm and 0.0741. The *SOBEL\_CAE* models showed underperforming results with the greatest variances for both metrics in every experiment.

Among the models trained with the combined dataset, *corr\_std* models, which showed the best performances, are tested on FYI and MYI test datasets (Table 4). The average RMSE and  $R^2$  score showed poorer performance on the FYI test dataset compared to the *CAE* models trained using the FYI training dataset. Conversely, the models trained using the combined dataset outperformed the *CAE* models for MYI datasets.

Table 4. Comparisons between sea ice surface roughness models trained using the FYI/MYI dataset and the combined dataset tested on FYI and MYI datasets.

	Test on FYI		Test on MYI	
	<i>corr_std</i> on combined dataset	<i>CAE</i> on FYI dataset	<i>corr_std</i> on combined dataset	<i>CAE</i> on MYI dataset
Average RMSE	45.70mm	43.03mm	73.81mm	78.72mm
Average $R^2$ score	0.0501	0.1640	-0.0602	-0.0776

### Thickness Regression

All models using 3D-CAE features show poorer RMSEs and  $R^2$  scores than other models in FYI thickness estimation (Figure 7). The three models with the lowest average RMSEs are *backscatter* (0.4609m), *corr\_std* (0.4591m) and *GLCM* (0.4594m). Respective average  $R^2$  scores are 0.1008, 0.1082 and 0.1066. The *canny\_CAE* is the best of all 3D-CAE models with average RMSE and  $R^2$  scores of 0.4802m and 0.0217. MYI thickness estimation results show a similar trend, where 3D-CAE models underperform other models. The *backscatter* models recorded the lowest average RMSE of 1.1007m and the highest average  $R^2$  score of 0.1457. For the combined dataset, tests results of *GLCM* models show the best performances with an average RMSE of 0.9306m and  $R^2$  score of 0.3092. The models that are trained separately on FYI and MYI datasets did not show improvements from the best models trained on the combined dataset (Table 5).

### 3D Convolutional Autoencoder (3D-CAE) Feature Engineering for Sea Ice Surface Roughness, Thickness and Type Extractions from RADARSAT-2 Synthetic Aperture Radar (SAR) Data

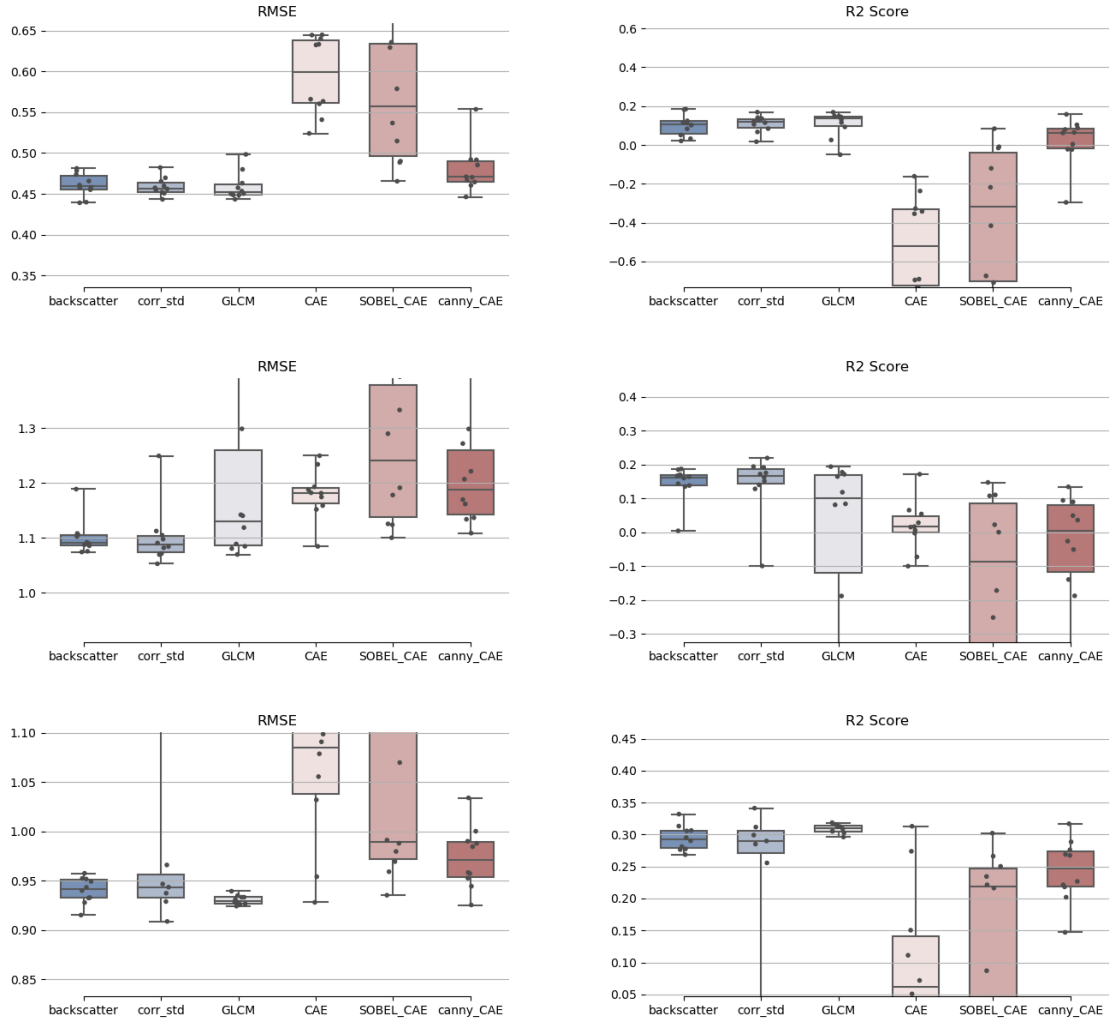


Figure 7. RMSEs (left) and  $R^2$  scores (right) of sea ice thickness regression models trained with FYI (top), MYI (middle) and combined (bottom) datasets.

Table 5. Comparisons between sea ice thickness models trained using the FYI/MYI dataset and the combined dataset tested on FYI and MYI datasets.

	Test on FYI		Test on MYI	
	<i>GLCM</i> on combined dataset	<i>corr_std</i> on FYI dataset	<i>GLCM</i> on combined dataset	<i>backscatter</i> on MYI dataset
Average RMSE	0.4499m	0.4591m	1.088m	1.1007m
Average $R^2$ score	0.1438	0.1082	0.1665	0.1457

## Discussion

The information losses from autoencoding with the developed 3D-CAEs are satisfactory with about ~90% of the data preservation. Since autoencoding is an unsupervised learning technique, the encoding-decoding processes on four-window stacks degrading the data preservation performance from six-window stacks are unexplainable. Nevertheless, edge detection windows appended to the latter windows are the 2D-convolutional products derived from HH and HV windows, and it is assumed that performing convolution the windows could have simplified the autoencoding process, resulting in a lower MAE.

Observations suggest significant effects of 3D-CAE features on improving FYI-MYI classification and FYI surface roughness regression performances. Especially, the success in the sea ice type classification using the 3D-CAE features trained with HH, HV, incidence angle, and Canny edge detection (Stack 3) is promising with a 3.7% accuracy improvement from the GLCM method discovered by Ressel et al. (2015). The small variance in the *canny\_CAE* results also makes it a more reliable method. When Sobel and Canny edge detection methods are compared, it is highly suggested that using Canny edge detection in training 3D-CAE features is the optimal practice as it outperformed *SOBEL\_CAE* results in every experiment. Models trained on the combined datasets performed better than those trained separately on FYI and MYI datasets on each of the respective estimations except for the FYI surface roughness test. If one could come up with a method that works better on separate FYI and MYI datasets, it would be an optimal practice to classify sea ice data into FYI and MYI with a *canny\_CAE* model before predicting the sea ice features.

The poor performances of 3D-CAE features on sea ice thickness leave further exploration of other methods. Landy et al. (2020) suggest sea ice surface roughness as a critical factor that can help estimate sea ice freeboard with CroySat-2 data. According to the authors, the potential error by disregarding the information can range up to 20% for FYI and 30% for MYI. Future studies may experiment with feeding surface roughness estimation results into training thickness regression. A deep learning method, the Siamese Network, is suggested to improve existing models. The architecture consists of two networks accepting two inputs sharing weights joined by the same function (Liu et al., 2019). It is effective when the two inputs share similarities from the same source, which would be the case of HH and HV polarizations. Additionally, segment-wise methods can take advantage of the object's spatial, textural and contextual properties along with the original spectral data (Liu and Xia, 2010; Wan et al., 2019). Although an attempt to approximate the real average surface roughness and thickness was made, there is a limitation that linearly collected data cannot represent the actual expert data due to spatial autocorrelation. Deep super-resolution methods could be a solution to mitigate such a problem. Multiple studies have used deep learning to obtain a finer resolution from coarse resolution images in the Computer Vision field (Dong et al., 2016; Lai et al., 2019; Lim et al., 2017; Shi et al., 2016). A study explored the application of the technology in SAR remote sensing (Shen et al., 2020).

### **Conclusion**

Attempts to enhance the sea ice surface roughness and thickness extractions were made applying deep learning technology of 3D-CAE feature engineering with RADARSAT-2 data, which are more abundant but generally perform poorer than altimetry data. The success of this study would introduce the potential applicability of the recently launched RADARSAT Constellation Mission (RCM) data in sea ice research. The 3D-CAE feature engineering method coupled with a Deep Neural Network showed improved performances in sea ice type classification and First-Year Ice surface roughness estimation from other kernel-based techniques experimented with in previous studies. Although their effectiveness was minimal or negative in sea ice thickness extraction, 3D-CAE features can potentially be useful if a thickness model that works better on separate FYI and MYI datasets is developed. Potential improvements are suggested based on the findings and previous knowledge from other studies. Future studies should focus on the effect of surface roughness in thickness ext, a state-of-the-art Siamese Network with HH and HV polarizations, object-wise approaches, and deep super-resolution techniques. This study's role in the field of remote sensing is an initiative work for further improvements in the SAR application for sea ice research, and the promising results can assist the development of more sophisticated technology.

### **Acknowledgements**

This project was not possible without Dr. Randall Scharien's guidance, who provided the data and supervision that this project is based on. It includes the instruction of foundation knowledge and insights into sea ice physics and SAR characteristics. The provision of expert data for FYI and MYI classification made an important transition in the study direction possible. Additionally, all ICE lab members are appreciated for their assistance. Lastly, the University of Victoria's Geomatics program should be acknowledged for its high-quality education, which provided the precious opportunity to conduct an interdisciplinary project.

## References

- Ahmed, A. S. (2018). Comparative study among Sobel, Prewitt and Canny edge detection operators used in image processing. *Journal of Theoretical and Applied Information Technology*, 96(19), 6517–6525.
- Cafarella, S. M., Scharien, R., Geldsetzer, T., Howell, S., Haas, C., Segal, R., & Nasonova, S. (2019). Estimation of Level and Deformed First-Year Sea Ice Surface Roughness in the Canadian Arctic Archipelago from C- and L-Band Synthetic Aperture Radar. *Canadian Journal of Remote Sensing*, 45(3–4), 457–475. [doi.org/10.1080/07038992.2019.1647102](https://doi.org/10.1080/07038992.2019.1647102)
- Dong, C., Loy, C. C., & Tang, X. (2016). Accelerating the Super-Resolution Convolutional Neural Network. *Computer Vision – ECCV 2016*, 391–407. [doi.org/10.1007/978-3-319-46475-6\\_25](https://doi.org/10.1007/978-3-319-46475-6_25)
- Haralick, R. M., Shanmugam, K., & Dinstein, I. (1973). Textural Features for Image Classification. *IEEE Transactions on Systems, Man, and Cybernetics*, SMC-3(6), 610–621. [doi.org/10.1109/tsmc.1973.4309314](https://doi.org/10.1109/tsmc.1973.4309314)
- Heaton, J. (2017). *The Number of Hidden Layers*. Heaton Research. [www.heatonresearch.com/2017/06/01/hidden-layers.html](http://www.heatonresearch.com/2017/06/01/hidden-layers.html)
- Karvonen, J., Cheng, B., Vihma, T., Arkett, M., & Carrieres, T. (2012). A method for sea ice thickness and concentration analysis based on SAR data and a thermodynamic model. *The Cryosphere*, 6(6), 1507–1526. [doi.org/10.5194/tc-6-1507-2012](https://doi.org/10.5194/tc-6-1507-2012)
- Kim, J. W., Kim, D. J., & Hwang, B. J. (2012). Characterization of Arctic Sea Ice Thickness Using High-Resolution Spaceborne Polarimetric SAR Data. *IEEE Transactions on Geoscience and Remote Sensing*, 50(1), 13–22. [doi.org/10.1109/tgrs.2011.2160070](https://doi.org/10.1109/tgrs.2011.2160070)
- Kwok, R., Cunningham, G. F., Wensnahan, M., Rigor, I., Zwally, H. J., & Yi, D. (2009). Thinning and volume loss of the Arctic Ocean sea ice cover: 2003–2008. *Journal of Geophysical Research*, 114(C7). [doi.org/10.1029/2009jc005312](https://doi.org/10.1029/2009jc005312)
- Lai, W. S., Huang, J. B., Ahuja, N., & Yang, M. H. (2019). Fast and Accurate Image Super-Resolution with Deep Laplacian Pyramid Networks. *IEEE Transactions on Pattern Analysis and Machine Intelligence*, 41(11), 2599–2613. [doi.org/10.1109/tpami.2018.2865304](https://doi.org/10.1109/tpami.2018.2865304)
- Landy, J. C., Petty, A. A., Tsamados, M., & Stroeve, J. C. (2020). Sea Ice Roughness Overlooked as a Key Source of Uncertainty in CryoSat-2 Ice Freeboard Retrievals. *Journal of Geophysical Research: Oceans*, 125(5). [doi.org/10.1029/2019jc015820](https://doi.org/10.1029/2019jc015820)
- Lee, S., Im, J., Kim, J., Kim, M., Shin, M., Kim, H. C., & Quackenbush, L. (2016). Arctic Sea Ice Thickness Estimation from CryoSat-2 Satellite Data Using Machine Learning-Based Lead Detection. *Remote Sensing*, 8(9), 698. [doi.org/10.3390/rs8090698](https://doi.org/10.3390/rs8090698)
- Lim, B., Son, S., Kim, H., Nah, S., & Mu Lee, K. (2017). Enhanced deep residual networks for single image super-resolution. In *Proceedings of the IEEE conference on computer vision and pattern recognition workshops* (pp. 136–144).



- Liu, D., & Xia, F. (2010). Assessing object-based classification: advantages and limitations. *Remote Sensing Letters*, 1(4), 187–194. [doi.org/10.1080/01431161003743173](https://doi.org/10.1080/01431161003743173)
- Liu, H., Guo, H., & Zhang, L. (2015). SVM-Based Sea Ice Classification Using Textural Features and Concentration From RADARSAT-2 Dual-Pol ScanSAR Data. *IEEE Journal of Selected Topics in Applied Earth Observations and Remote Sensing*, 8(4), 1601–1613. [doi.org/10.1109/jstars.2014.2365215](https://doi.org/10.1109/jstars.2014.2365215)
- Liu, X., Zhou, Y., Zhao, J., Yao, R., Liu, B., & Zheng, Y. (2019). Siamese Convolutional Neural Networks for Remote Sensing Scene Classification. *IEEE Geoscience and Remote Sensing Letters*, 16(8), 1200–1204. [doi.org/10.1109/lgrs.2019.2894399](https://doi.org/10.1109/lgrs.2019.2894399)
- Petty, A. A., Kurtz, N. T., Kwok, R., Markus, T., & Neumann, T. A. (2020). Winter Arctic Sea Ice Thickness From ICESat-2 Freeboards. *Journal of Geophysical Research: Oceans*, 125(5). [doi.org/10.1029/2019jc015764](https://doi.org/10.1029/2019jc015764)
- Ressel, R., Frost, A., & Lehner, S. (2015). A Neural Network-Based Classification for Sea Ice Types on X-Band SAR Images. *IEEE Journal of Selected Topics in Applied Earth Observations and Remote Sensing*, 8(7), 3672–3680. [doi.org/10.1109/jstars.2015.2436993](https://doi.org/10.1109/jstars.2015.2436993)
- Shang, R., Wang, G., A. Okoth, M., & Jiao, L. (2019). Complex-Valued Convolutional Autoencoder and Spatial Pixel-Squares Refinement for Polarimetric SAR Image Classification. *Remote Sensing*, 11(5), 522. [doi.org/10.3390/rs11050522](https://doi.org/10.3390/rs11050522)
- Shi, W., Caballero, J., Huszár, F., Totz, J., Aitken, A. P., Bishop, R., ... & Wang, Z. (2016). Real-time single image and video super-resolution using an efficient sub-pixel convolutional neural network. In *Proceedings of the IEEE conference on computer vision and pattern recognition* (pp. 1874-1883).
- Shen, H., Lin, L., Li, J., Yuan, Q., & Zhao, L. (2020). A residual convolutional neural network for polarimetric SAR image super-resolution. *ISPRS Journal of Photogrammetry and Remote Sensing*, 161, 90–108. [doi.org/10.1016/j.isprsjprs.2020.01.006](https://doi.org/10.1016/j.isprsjprs.2020.01.006)
- Su, N., Zhang, C., Yan, Y., Zhao, C., & Tan, Z. (2018). Sea-Ice Image Classification for Channel Navigation in Polar Application. *IGARSS 2018 - 2018 IEEE International Geoscience and Remote Sensing Symposium*. Published. [doi.org/10.1109/igarss.2018.8518191](https://doi.org/10.1109/igarss.2018.8518191)
- Vijayarani, S., & Vinupriya, M. (2013). Performance analysis of Canny and Sobel edge detection algorithms in image mining. *International Journal of Innovative Research in Computer and Communication Engineering*, 1(8), 1760-1767.
- Wan, L., Zhang, T., & You, H. (2019). Object-based method for optical and SAR images change detection. *The Journal of Engineering*, 2019(21), 7410–7414. [doi.org/10.1049/joe.2019.0620](https://doi.org/10.1049/joe.2019.0620)